IEEE Open Journal of
Antennas and Propagation

Received 6 September 2023; revised 16 October 2023; accepted 29 October 2023. Date of publication 2 November 2023;
date of current version 22 November 2023.

Digital Object Identifier 10.1109/OJAP.2023.3329767

UTD-Type Solution of Physical Optics Approximation for Reconfigurable Intelligent Surface Modeled by a Continuous Planar Surface

XIN DU (Member, IEEE), CHECHIA KANG, AND JUN-ICHI TAKADA (Senior Member, IEEE)

Department of Transdisciplinary Science and Engineering, Tokyo Institute of Technology, Tokyo 152-8550, Japan

CORRESPONDING AUTHOR: X. DU (e-mail: du.x.ab@m.titech.ac.jp)

This work was supported by the Commissioned Research through the National Institute of Information
and Communications Technology (NICT), Japan, under Grant #02701.

ABSTRACT An accurate and fast prediction technique is necessary for the radiation pattern of the reconfigurable intelligent surface (RIS) to quantitatively and efficiently evaluate the performance of RIS. Based on the uniform theory of diffraction (UTD), this paper proposes a UTD-type solution of the physical optics approximation (PO) for RIS modeled by a continuous planar surface in a two-dimensional environment. The authors validate the proposal under different scenarios in an indoor environment ($0.1-20$ m) at the terahertz bands ($100-300$ GHz), by comparing them with those computed using the Fresnel approximation, the Fraunhofer approximation, PO, and the full-wave approach based on the method of moment (MoM). The simulated results show that compared to MoM, the proposal and PO achieve good accuracy with a smaller error of less than 1 dB, while the Fresnel and Fraunhofer approximations present imperfect accuracy with an error of larger than 1 dB in the near-field region. Moreover, the proposal outperforms the PO in terms of faster calculation time by approximately $70\% - 76\%$, and the computational time of the proposal is improved by approximately $46,190 - 125,460$ times compared to MoM. Furthermore, the computational complexities of the proposal, the Fresnel approximation and the Fraunhofer approximation are $O(N^0)$, compared to that of PO and MoM by $O(N)$ and $O(N^2)$, respectively, where N and $O(\cdot)$ are the number of sampling points and the notation of order, respectively. Therefore, the proposal can achieve a good balance between accuracy and computational cost.

INDEX TERMS Electromagnetic model, numerical simulation, physical optics, reconfigurable intelligent surface, terahertz, uniform theory of diffraction.

I. INTRODUCTION

TOWARD the future sixth-generation (6G) wireless communication system, new technologies are required to meet the extremely high cost of ultra-dense networking and ubiquitous massive multiple-input multiple-output (MIMO) at the terahertz (THz) bands in the smart radio environment [1], [2]. Reconfigurable intelligent surface (RIS) is one of the unprecedented and revolutionary solutions due to its lower hardware cost, low energy consumption, flexible deployment, and quick response [3], [4], [5]. The metasurface technology has enabled the design of RISs that can direct radio waves in a desired direction. By carefully and accurately designing the phase shift of each element, the shadowing effect can be reduced [6], [7], as demonstrated in Fig. 1. This is made possible because of the transformative nature of the metasurface, which allows for an arbitrary phase distribution within the reflector. Therefore, an accurate and fast electromagnetic (EM) model is needed to quantitatively and efficiently evaluate the performance of RIS [8], [9].

Several efforts have been devoted to establishing EM models for RIS. The work in [10] calculated the link budget of the RIS by the sum-distance law using the two-path model, although this is not a realistic calculation approach because the sum-distance law is only applicable when the reflector is infinite. The work in [11] proposed the product-distance law considering the finite size of the reflector; however, it does not satisfy the law of energy conservation. The sum-distance law assumes RIS as an infinitely large mirror to calculate the

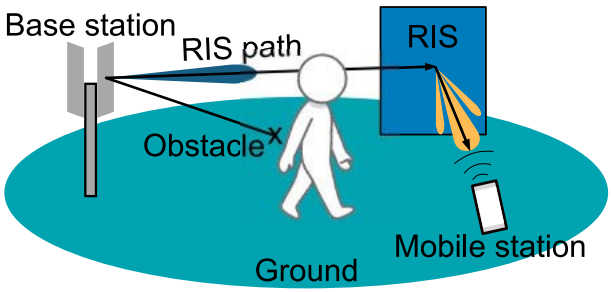

FIGURE 1. Mitigation of the shadowing effect by using RIS. The main lobe of the radiation pattern is toward the desired reflection direction adjusted by RIS, while the side lobe may cause unwanted ISI.

specular reflection. On the other hand, the product-distance law calculates the scattered field considering that RIS is a finitely large scatterer and is sufficiently small compared to the propagation distance. In the sum-distance law, the energy decreases with the square of the distance, in contrast to the fourth power of the distance for the product-distance law. The works in [8], [12], [13], [14] discussed in detail the near-field and far-field formulations with mirrors and scatterers. In [8], it was introduced that the energy is inversely proportional to the square and the fourth power of the distance for the near-field and far-field cases, respectively. The work in [12] used the scalar diffraction theory to prove that the sum-distance and product-distance laws hold in the near and far fields, respectively. In the paper [13], along with verification experiments, it is concluded that the sum-distance and product-distance laws hold for near-field broadcasting and far-field beamforming, respectively. In the paper [14], the relation between the sum-distance and product-distance laws was introduced. However, in these studies, although the distance from each RIS element to the antenna is varied, the received power increases steadily with an increase in the number of each element, and hence the law of energy conservation is not satisfied.

In the papers [15], [16], not only the distance from each element to the antenna but also the effective antenna area was varied. Accordingly, even if the number of elements is increased, the received power converges and satisfies the law of energy conservation. The works in [17], [18] further considered the effects of polarization for RIS. The work in [18] proposed a power scaling law for the MIMO-relay-RIS channel by merging the findings in [15] and [19], which derived link budget formulations for the MIMO-RIS and relay-RIS models, respectively. Although the works in [15], [17], [18], [19] consider both the law of energy conservation and the effects of polarization, they cannot give the radiation pattern of RIS. In these papers, the observation angle is always identical to the angle of the desired reflection direction adjusted by RIS, henceforth the works in [15], [17], [18], [19] can only calculate the peak value at the main lobe of the RIS radiation pattern. Comprehending the peak value may be sufficient to formulate the link budget. However, knowing the radiation pattern of RIS is important to predict the side-lobe level [20], [21], where unwanted emissions may cause small-scale fading or inter-system-interference (ISI) [22].

The work in [23] proposed a general macroscopic model, which can provide the RIS radiation pattern and was validated against full-wave simulations and measurements. Nevertheless, this was a semi-empirical model and may require parameter adjustment with the experimental data. The works in [24] proposed deterministic models based on the physical optics approximation (PO) [25], [26], which can also provide the radiation pattern of RIS. In the PO calculation, the field scattered from RIS can be easily calculated by the integral of the approximated surface current weighted by the phase shift of RIS [24]. Unfortunately, the traditional PO expressed by numerical integration is impractical, since it requires a large computational load, compared to the analytical approach [27]. Thus, the paper [24] involved the Fraunhofer and Fresnel approximations (see Appendix A) in the PO calculation to obtain analytical solutions, resulting in a lower computational cost. However, as mentioned in Appendix A, the Fraunhofer and Fresnel approximations are only applicable in the Fraunhofer and Fresnel regions, respectively, and they are not valid in the near-field region. Here, we consider an indoor scenario at THz, where RIS with a maximum width of 0.5 m is placed in an office environment at 300 GHz. According to the condition (52) mentioned in Appendix A, the boundary of the near-field region is approximately 5 m further away from RIS. Since there are quite cases for a user close to RIS within such a distance in an indoor environment, the Fraunhofer and Fresnel approximations in [24] may not be sufficient to accurately predict the radiation pattern of RIS in the near-field region at THz toward the 6G wireless communication system.

The disadvantages of the Fraunhofer and Fresnel approximations in the near-field region have motivated the establishment of an accurate method based on the uniform theory of diffraction (UTD) [28], [29], [30], [31], [32], [33]. This paper aims to derive the UTD-type solution of PO for accurately and fast predicting the radiation pattern of RIS modeled by a continuous planar surface. Unlike the works in [36], [37], which derive the UTD-type solution of PO for a locally periodic metasurface, this work proposes a novel formulation for RIS modeled by a continuous planar surface. This assumption is beneficial to easily and quickly calculate the radiation pattern [14] without the sophisticated and dedicated reflection-points search steps of the works [36], [37], where a locally periodic metasurface can contain multiple reflection points [36]. Unlike the work in [38], which focuses on end-to-end mutual coupling RIS-assisted wireless systems, this work concentrates on the radiation pattern of RIS. Moreover, this paper performs full-wave validation in comparison to the works in [36], [38]. Furthermore, to the best of the authors' knowledge, this study is the first to compare and discuss the computational time of the proposed method, the traditional PO, the Fraunhofer approximation of PO, the Fresnel approximation of PO, and the full-wave method.

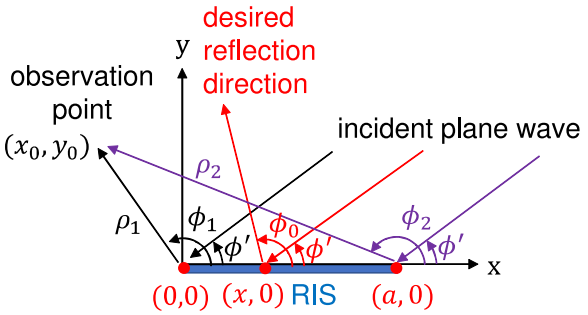

FIGURE 2. Model of RIS (top view).

In this work, the UTD-type solution of PO for RIS is proposed and validated against the traditional PO, the Fraunhofer approximation of PO, the Fresnel approximation of PO, and the full-wave approach based on the moment method (MoM) [34], [35] in a two-dimensional (2D) environment. Compared to other works, this approach can produce a fast and accurate prediction of the RIS radiation pattern in, not only the Fraunhofer and Fresnel regions, but also the near-field region. The remainder of this paper is organized as follows. The proposed method is explained in Section II. The validated methods and simulated results are presented and discussed in Section III. The applications of the proposal are described in Section IV. Finally, Section V concludes this work and discusses the limitations of this work, as well as future work.

II. PROPOSAL

This section derives the UTD-type solution of PO for the scattering from RIS. 2D problem is considered by assuming that the problem scenario is uniform along the z-axis. As shown in Fig. 2, RIS with a width of a is located on the x-axis, where the origin is placed at the left edge of the RIS. For simplicity, a uniform plane wave with perpendicular polarization is assumed to travel in the direction of $(-\cos\phi', -\sin\phi')$. The parameters ϕ_1 and ϕ_2 are the angles of the left and right diffracted rays measured from the x-axis, respectively. Parameters ρ_1 and ρ_2 are the distances from the observation point (x_0, y_0) to the left and right diffraction points, respectively. Viz.

$$x_0 = \rho_1 \cos\phi_1 = \rho_2 \cos\phi_2 + a, \tag{1a}$$
$$y_0 = \rho_1 \sin\phi_1 = \rho_2 \sin\phi_2. \tag{1b}$$

The z component of the incident electric field E_z^i and the x, y components of the incident magnetic field $H_{x,y}^i$ at the arbitrary point $(x, 0)$ of RIS $(0 \le x \le a)$ are calculated as

$$E_z^i(x) = E_0 e^{jk_0 x\cos\phi'}, \tag{2a}$$
$$H_x^i(x) = -\frac{E_0}{\eta}\sin\phi' e^{jk_0 x\cos\phi'}, \tag{2b}$$
$$H_y^i(x) = \frac{E_0}{\eta}\cos\phi' e^{jk_0 x\cos\phi'} \tag{2c}$$

where E_0, η, and k_0 are the z component of the incident electric field at the origin, impedance, and wave number in free space, respectively.

In the PO assumption, the surface current $\boldsymbol{J}^{PO}$ is considered as

$$\begin{aligned}\boldsymbol{J}^{PO}(x) &= 2\hat{y} \times \left(H_x^i(x)\hat{x} + H_y^i(x)\hat{y}\right) \\ &= \frac{2E_0}{\eta}\sin\phi' e^{jk_0 x\cos\phi'}\hat{z}.\end{aligned} \tag{3}$$

where $\hat{x}$, $\hat{y}$, and $\hat{z}$ are the unit vectors of the x, y, and z directions, respectively.

The desired reflection direction of RIS is supported at the angle of ϕ_0 measured from the x-axis. According to [24], by assuming that the element of RIS is sufficiently small and considering that the scattered waves from all the elements need to be added constructively, the phase shift $\xi(x)$ at $(x, 0)$ is designed as

$$\xi(x) = e^{-jk_0 x(\cos\phi_0 + \cos\phi')}. \tag{4}$$

The z component of the scattered electric field E_z^s is obtained by the integral of the z component of the surface current $J_z^{PO}(x)$ giving a phase shift $\xi(x)$ weighted by a free-space Green function $G(x)$ as

$$\begin{aligned}E_z^s &= -j\omega\mu\int_0^a J_z^{PO}(x)\xi(x)G(x)dx \\ &= -\frac{k_0 E_0\sin\phi'}{2}\int_0^a e^{-jk_0 x\cos\phi_0}H_0^{(2)}(k_0\rho(x))dx\end{aligned} \tag{5}$$

with

$$\rho(x) = \sqrt{(x_0 - x)^2 + y_0^2} \tag{6}$$

where $H_0^{(2)}(\cdot)$, $\rho(x)$, ω, and μ are the second kind of the Hankel function for the zeroth order corresponding to the 2D free-space green function, distance from the arbitrary point $(x, 0)$ of RIS to Rx, angular frequency, and permeability, respectively. Here, the angular spectral representation of the Hankel function [39] is applied as

$$H_0^{(2)}(k_0\rho(x)) = \frac{1}{\pi}\int_{-\infty}^{\infty}\frac{e^{-j(k_x(x_0 - x) + k_y|y_0|)}}{k_y}dk_x \tag{7}$$

with

$$k_y = \begin{cases} +\sqrt{k_0^2 - k_x^2}, & (|k_x| \le k_0) \\ -j\sqrt{k_x^2 - k_0^2}, & (|k_x| > k_0) \end{cases} \tag{8}$$

where k_x and k_y are the parameters of the angular spectral domain corresponding to the x-space and y-space domains, respectively [40], [41], [42], [43]. Considering $y_0 > 0$ for the backward scattering and substituting (7) into (5), we have

$$\begin{aligned}E_z^s = &-\frac{k_0 E_0\sin\phi'}{2\pi}\int_0^a e^{-jk_0 x\cos\phi_0} \\ &\times \int_{-\infty}^{\infty}\frac{e^{-j(k_x(x_0 - x) + k_y y_0)}}{k_y}dk_x dx.\end{aligned} \tag{9}$$

By interchanging the order of integration and using the integration formula as

$$\int_0^a e^{-\mathrm{j}k_0 x\cos\phi_0} e^{\mathrm{j}k_x x}\mathrm{d}x = \frac{\mathrm{j}\left(1-e^{\mathrm{j}k_x a-\mathrm{j}k_0 a\cos\phi_0}\right)}{k_x - k_0\cos\phi_0}, \quad (10)$$

the integral (9) becomes

$$\begin{aligned} E_z^s &= -\frac{k_0 E_0 \sin\phi'}{2\pi} \\ &\quad\times \int_{-\infty}^{\infty} \frac{\mathrm{j}\left(1-e^{\mathrm{j}k_x a-\mathrm{j}k_0 a\cos\phi_0}\right)}{k_x - k_0\cos\phi_0} \frac{e^{-\mathrm{j}(k_x x_0+k_y y_0)}}{k_y}\mathrm{d}k_x \\ &= E_1^s - E_2^s \end{aligned} \quad (11)$$

with

$$E_1^s = -\frac{k_0 E_0 \sin\phi'}{2\pi}\int_{-\infty}^{\infty} \frac{\mathrm{j}e^{-\mathrm{j}(k_x x_0+k_y y_0)}}{(k_x - k_0\cos\phi_0)k_y}\mathrm{d}k_x, \quad (12a)$$

$$\begin{aligned} E_2^s &= -\frac{k_0 E_0 e^{-\mathrm{j}k_0 a\cos\phi_0}\sin\phi'}{2\pi} \\ &\quad\times \int_{-\infty}^{\infty} \frac{\mathrm{j}e^{-\mathrm{j}(k_x(x_0-a)+k_y y_0)}}{(k_x - k_0\cos\phi_0)k_y}\mathrm{d}k_x \end{aligned} \quad (12b)$$

where E_1^s and E_2^s are the complex amplitudes of the scattered electric fields contributed from the left and right edges of RIS, respectively. By applying (1) and letting

$$k_x = k_0\cos k_\phi, \quad k_y = k_0\sin k_\phi, \quad (13a)$$

$$x_1 = 0, \quad x_2 = a, \quad (13b)$$

the integrals in (12a) and (12b) become

$$\begin{aligned} E_1^s &= \frac{\mathrm{j}E_0\sin\phi'}{2\pi}\int_\Gamma \frac{e^{-\mathrm{j}k_0\rho_1\cos(\phi_1-k_\phi)}}{\cos k_\phi - \cos\phi_0}\mathrm{d}k_\phi \\ &= \frac{\mathrm{j}E_z^i(x_1)\xi(x_1)\sin\phi'}{2\pi}\int_\Gamma \frac{e^{-\mathrm{j}k_0\rho_1\cos(\phi_1-k_\phi)}}{\cos k_\phi - \cos\phi_0}\mathrm{d}k_\phi, \end{aligned} \quad (14a)$$

$$\begin{aligned} E_2^s &= \frac{\mathrm{j}E_0 e^{-\mathrm{j}k_0 a\cos\phi_0}\sin\phi'}{2\pi}\int_\Gamma \frac{e^{-\mathrm{j}k_0\rho_2\cos(\phi_2-k_\phi)}}{\cos k_\phi - \cos\phi_0}\mathrm{d}k_\phi \\ &= \frac{\mathrm{j}E_z^i(x_2)\xi(x_2)\sin\phi'}{2\pi}\int_\Gamma \frac{e^{-\mathrm{j}k_0\rho_2\cos(\phi_2-k_\phi)}}{\cos k_\phi - \cos\phi_0}\mathrm{d}k_\phi \end{aligned} \quad (14b)$$

where Γ is the integration path in the complex k_ϕ domain, as shown in Fig. 3. Variables $k_x = 0$, $k_x = \infty$, and $k_x = -\infty$ transform into $k_\phi = \pi/2$, $k_\phi = -\mathrm{j}\infty$, and $k_\phi = \pi + \mathrm{j}\infty$, respectively. By unifying (14a) and (14b), we have

$$\begin{aligned} E_{1,2}^s &= \frac{\mathrm{j}E_z^i(x_{1,2})\xi(x_{1,2})}{4\pi}\frac{\sin\phi'}{\sin\phi_0} \\ &\quad\times \int_\Gamma \left(\cot\frac{k_\phi+\phi_0}{2} - \cot\frac{k_\phi-\phi_0}{2}\right) \\ &\quad\times e^{-\mathrm{j}k_0\rho_{1,2}\cos(\phi_{1,2}-k_\phi)}\mathrm{d}k_\phi. \end{aligned} \quad (15)$$

The integrals in (15) cannot be directly solved in a closed form. Since the integrand far away from the stationary phase point (SPP) oscillates rapidly, the method of stationary phase can be applied to approximate the integral [34]. $\mathrm{SPP}_{1,2}$ for $E_{1,2}^s$ can be calculated as

$$\frac{\mathrm{d}}{\mathrm{d}k_\phi}\left(-\cos\left(\phi_{1,2}-k_\phi\right)\right) = 0 \;\Rightarrow\; k_\phi = \phi_{1,2}. \quad (16)$$

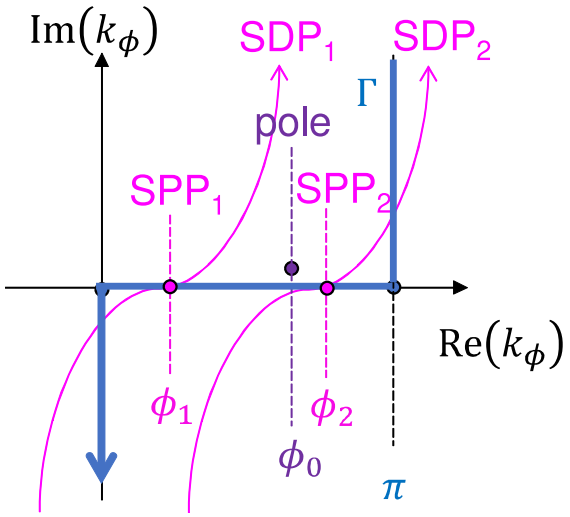

FIGURE 3. Complex k_ϕ plane. An example: a case of $\phi_1 < \phi_0 < \phi_2$.

The integrals over the steepest descent paths ($\mathrm{SDP}_{1,2}$) passing through $\mathrm{SPP}_{1,2}$ at $\phi_{1,2}$ shown in Fig. 3 can be evaluated by the Pauli-Clemmow modified method of steepest descent [44] as

$$\begin{aligned} &\int_{\mathrm{SDP}_{1,2}} \cot\frac{k_\phi \pm \phi_0}{2} e^{-\mathrm{j}k_0\rho_{1,2}\cos(\phi_{1,2}-k_\phi)}\mathrm{d}k_\phi \\ &= \sqrt{\frac{2\pi}{k_0\rho_{1,2}}}\frac{e^{-\mathrm{j}(k_0\rho_{1,2}-\frac{\pi}{4})}}{\tan\left((\phi_{1,2}\pm\phi_0)/2\right)} F\left(2k_0\rho_{1,2}\sin^2\frac{\phi_{1,2}\pm\phi_0}{2}\right) \end{aligned} \quad (17)$$

where integrals over SDP_1 and SDP_2 correspond to the contributions of the left and right diffracted fields, respectively. The function $F(\cdot)$ is mentioned in Appendix B.

Although the integrands in (15) have infinite poles at $\pm\phi_0 + 2n\pi$ ($n \in \mathbb{Z}$), the pole at ϕ_0 corresponding to the reflected field is chosen for residue evaluation, since its real part belongs to the region of interest with $[0, \pi]$. Actually, the pole at ϕ_0 has a positive imaginary part, as shown in Fig. 3. The proof is given as follows:

For obtaining the convergence results in the case of $a \to \infty$, the integrand in (10) must vanish at $x \to \infty$ [45]. Thus, the complex exponential factor in (10) has to become a decay exponential factor. Therefore, $k_x - k_0\cos\phi_0$ should have a positive imaginary part as

$$\mathrm{Im}(k_x - k_0\cos\phi_0) > 0 \;\Rightarrow\; \mathrm{Im}\left(\cos k_\phi\right) > \mathrm{Im}(\cos\phi_0). \quad (18)$$

Here, the trigonometric formula is applied as

$$\begin{aligned} \cos z &= \cos\left(\mathrm{Re}(z)\right)\cosh\left(\mathrm{Im}(z)\right) \\ &\quad - \mathrm{j}\sin\left(\mathrm{Re}(z)\right)\sinh\left(\mathrm{Im}(z)\right) \end{aligned} \quad (19)$$

where $\mathrm{Re}(z)$ and $\mathrm{Im}(z)$ are the real and imaginary parts of an arbitrary complex number z, respectively. Thus, (18) becomes

$$\sin\left(\mathrm{Re}\left(k_\phi\right)\right)\sinh\left(\mathrm{Im}\left(k_\phi\right)\right) < \sin\left(\mathrm{Re}(\phi_0)\right)\sinh\left(\mathrm{Im}(\phi_0)\right). \quad (20)$$

When the real parts of k_ϕ and ϕ_0 are with the same value at $[0, \pi]$, we have

$$\begin{aligned}&\sinh\left(\mathrm{Im}\left(k_\phi\right)\right) < \sinh\left(\mathrm{Im}(\phi_0)\right)\\ &\Rightarrow \mathrm{Im}(\phi_0) > \mathrm{Im}\left(k_\phi\right) = 0 \quad \text{for} \quad \mathrm{Re}\left(k_\phi\right) \in [0, \pi]. \end{aligned} \tag{21}$$

Therefore, the pole at ϕ_0 has a positive imaginary part.

The closed contour integral over Γ and $\mathrm{SDP}_{1,2}$ can be evaluated by the residue of the pole at ϕ_0 enclosed by Γ and $\mathrm{SDP}_{1,2}$ as

$$\begin{aligned}&\left(\int_\Gamma + \int_{\mathrm{SDP}_{1,2}}\right)\left(\cot\frac{k_\phi+\phi_0}{2} - \cot\frac{k_\phi-\phi_0}{2}\right)\\ &\quad\times\ e^{-\mathrm{j}k_0\rho_{1,2}\cos\left(\phi_{1,2}-k_\phi\right)}\mathrm{d}k_\phi\\ &= \begin{cases} -\mathrm{j}2\pi\,\mathrm{Res}_{1,2}, & \left(\phi_{1,2} < \phi_0\right)\\ 0, & \left(\phi_{1,2} > \phi_0\right)\end{cases}\end{aligned} \tag{22}$$

where Res_1 and Res_2 denote the residues of the pole corresponding to SDP_1 and SDP_2, respectively. The residues are evaluated as

$$\begin{aligned}\mathrm{Res}_{1,2} &= \lim_{k_\phi\to\phi_0}\left(k_\phi-\phi_0\right)\left(\cot\frac{k_\phi+\phi_0}{2} - \cot\frac{k_\phi-\phi_0}{2}\right)\\ &\quad\times\ e^{-\mathrm{j}k_0\rho_{1,2}\cos\left(\phi_{1,2}-k_\phi\right)}\\ &= -2e^{-\mathrm{j}k_0\rho_{1,2}\cos\left(\phi_{1,2}-\phi_0\right)}.\end{aligned} \tag{23}$$

By substituting (17) and (23) into (22), $E^{\mathrm{s}}_{1,2}$ in (15) can be separated as

$$E^{\mathrm{s}}_{1,2} = \begin{cases} E^{\mathrm{r}}_{1,2} + E^{\mathrm{d}}_{1,2}, & \left(\phi_{1,2} < \phi_0\right)\\ E^{\mathrm{d}}_{1,2}, & \left(\phi_{1,2} > \phi_0\right)\end{cases} \tag{24}$$

with

$$E^{\mathrm{d}}_{1,2} = E^{\mathrm{i}}_z\left(x_{1,2}\right)\xi\left(x_{1,2}\right)D^{\mathrm{RIS}}_\perp\left(\rho_{1,2}, \phi_{1,2}, \phi', \phi_0\right)\frac{e^{-\mathrm{j}k_0\rho_{1,2}}}{\sqrt{\rho_{1,2}}}, \tag{25a}$$

$$E^{\mathrm{r}}_{1,2} = E^{\mathrm{i}}_z\left(x_{1,2}\right)\xi\left(x_{1,2}\right)R^{\mathrm{RIS}}_\perp\left(\phi', \phi_0\right)e^{-\mathrm{j}k_0\rho_{1,2}\cos\left(\phi_{1,2}-\phi_0\right)} \tag{25b}$$

where $E^{\mathrm{d}}_{1,2}$ and $E^{\mathrm{r}}_{1,2}$ denote the complex amplitudes of the diffracted and reflected electric fields, respectively. The uniform PO diffraction coefficient $D^{\mathrm{RIS}}_\perp$ and reflection coefficient $R^{\mathrm{RIS}}_\perp$ for the scattering from RIS in perpendicular polarization are proposed as

$$\begin{aligned}D^{\mathrm{RIS}}_\perp\left(\rho, \phi, \phi', \phi_0\right) &= \frac{-e^{-\mathrm{j}\frac{\pi}{4}}\sin\phi'}{\sqrt{8\pi k_0}\sin\phi_0}\\ &\quad\times\left(\cot\frac{\phi-\phi_0}{2}F\left(2k_0\rho\sin^2\frac{\phi-\phi_0}{2}\right)\right.\\ &\quad\left.-\cot\frac{\phi+\phi_0}{2}F\left(2k_0\rho\sin^2\frac{\phi+\phi_0}{2}\right)\right),\end{aligned} \tag{26a}$$

$$R^{\mathrm{RIS}}_\perp\left(\phi', \phi_0\right) = -\frac{\sin\phi'}{\sin\phi_0}. \tag{26b}$$

For parallel polarization, we succinctly show a similar derivation in Appendix C.

In the diffraction coefficients, $\cot\{(\phi_{1,2}-\phi_0)/2\}$ has the singularity at $\phi_{1,2} = \phi_0$. The value of $E^{\mathrm{s}}_{1,2}$ at $\phi_{1,2} = \phi_0$ is defined to be the limiting value as

$$\begin{aligned}&\lim_{\phi_{1,2}\to\phi_0+0} E^{\mathrm{d}}_{1,2} = \lim_{\phi_{1,2}\to\phi_0-0} E^{\mathrm{d}}_{1,2} + E^{\mathrm{r}}_{1,2} = \frac{1}{2}E^{\mathrm{r}}_{1,2}\\ &\Rightarrow \lim_{\phi_{1,2}\to\phi_0} E^{\mathrm{s}}_{1,2} = \frac{1}{2}E^{\mathrm{r}}_{1,2}.\end{aligned} \tag{27}$$

Note that the left-hand sides of (28a) and (28b) have the same result as

$$\begin{aligned}&E^{\mathrm{i}}_z(x_1)\xi(x_1)e^{-\mathrm{j}k_0\rho_1\cos\left(\phi_1-\phi_0\right)}\\ &\quad= E_0e^{-\mathrm{j}k_0(\rho_1\cos\phi_1\cos\phi_0+\rho_1\sin\phi_1\sin\phi_0)}\\ &\quad= E_0e^{-\mathrm{j}k_0((\rho_2\cos\phi_2+a)\cos\phi_0+\rho_2\sin\phi_2\sin\phi_0)},\end{aligned} \tag{28a}$$

$$\begin{aligned}&E^{\mathrm{i}}_z(x_2)\xi(x_2)e^{-\mathrm{j}k_0\rho_2\cos\left(\phi_2-\phi_0\right)}\\ &\quad= E_0e^{-\mathrm{j}k_0(\rho_2\cos\left(\phi_2-\phi_0\right)+a\cos\phi_0)}\\ &\quad= E_0e^{-\mathrm{j}k_0((\rho_2\cos\phi_2+a)\cos\phi_0+\rho_2\sin\phi_2\sin\phi_0)},\end{aligned} \tag{28b}$$

and hence E^{r}_1 and E^{r}_2 are equivalent. Let E^{r} represent either E^{r}_1 or E^{r}_2 as

$$E^{\mathrm{r}} = E^{\mathrm{r}}_1 = E^{\mathrm{r}}_2. \tag{29}$$

Although the direction of the angles of the rays at the left edge in this work is the same as the traditional UTD [28], [29], [30], [31], [32], [33], they are different for the right edge. In UTD [28], [29], [30], [31], [32], [33], the angles of the rays at the right edge are defined to start at π (negative x-axis) and to increase for rotations in clockwise orientation. However, in this work, the ray angles at the right edge are defined to start at 0 (positive x-axis) and rotate in counterclockwise orientation. To unify this work with UTD, we consider the complex amplitudes of the left diffracted field $E^{\mathrm{d}}_{\mathrm{L}}$ and the right diffracted field $E^{\mathrm{d}}_{\mathrm{R}}$ as

$$E^{\mathrm{d}}_{\mathrm{L}} = E^{\mathrm{i}}_z(x_1)\xi(x_1)D^{\mathrm{RIS}}_\perp\left(\rho_1, \phi_1, \phi', \phi_0\right)\frac{e^{-\mathrm{j}k_0\rho_1}}{\sqrt{\rho_1}} = E^{\mathrm{d}}_1, \tag{30a}$$

$$\begin{aligned}E^{\mathrm{d}}_{\mathrm{R}} &= E^{\mathrm{i}}_z(x_2)\xi(x_2)\\ &\quad\times\ D^{\mathrm{RIS}}_\perp\left(\rho_2, \pi-\phi_2, \pi-\phi', \pi-\phi_0\right)\frac{e^{-\mathrm{j}k_0\rho_2}}{\sqrt{\rho_2}}\\ &= -E^{\mathrm{d}}_2.\end{aligned} \tag{30b}$$

Here, the reflection coefficient $R^{\mathrm{RIS}}_\perp$ has no change despite the directions of the angles, owning to

$$R^{\mathrm{RIS}}_\perp\left(\pi-\phi', \pi-\phi_0\right) = R^{\mathrm{RIS}}_\perp\left(\phi', \phi_0\right). \tag{31}$$

Ultimately, from (24)-(30b), the complex amplitude of the scattered electric field in (11) is calculated by (32).

$$E^{\mathrm{s}}_z = \begin{cases} E^{\mathrm{d}}_{\mathrm{L}} + E^{\mathrm{d}}_{\mathrm{R}}, & \left(\phi_0 < \phi_1\right)\\ E^{\mathrm{d}}_{\mathrm{R}} + E^{\mathrm{r}}/2, & \left(\phi_0 = \phi_1\right)\\ E^{\mathrm{d}}_{\mathrm{L}} + E^{\mathrm{d}}_{\mathrm{R}} + E^{\mathrm{r}}, & \left(\phi_1 < \phi_0 < \phi_2\right)\\ E^{\mathrm{d}}_{\mathrm{L}} + E^{\mathrm{r}}/2, & \left(\phi_0 = \phi_2\right)\\ E^{\mathrm{d}}_{\mathrm{L}} + E^{\mathrm{d}}_{\mathrm{R}}, & \left(\phi_0 > \phi_2\right)\end{cases} \tag{32}$$

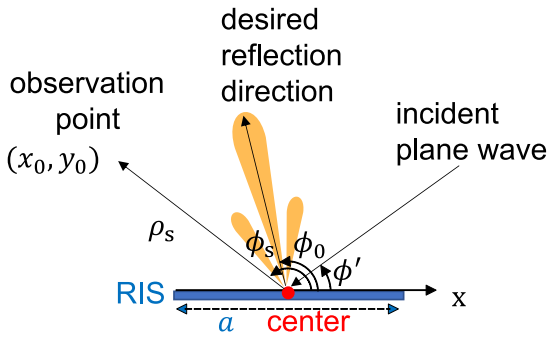

FIGURE 4. Simulation environment (top view).

III. SIMULATIONS

This section introduces the simulation environment, methods, scenarios, conditions, and parameters. According to Section II, the simulation environment is supposed to be uniform along the z-axis, as shown in Fig. 4, where ρ_s and ϕ_s are the distance and observation angle from the center of RIS to Rx, respectively. In this work, only the scattered field from RIS is used to evaluate the performance of RIS, by assuming that the incident field to the Rx and the reflected field from the wall are neglected.

Five methods are considered, i.e., the MoM, PO, Fraunhofer approximation, Fresnel approximation, and proposal. Specifically, MoM using the electric field integral equation is used as a reference of accuracy. In perpendicular polarization, the z component of the scattered electric field E_z^{MoM} from RIS can be calculated by using a phase shift $\xi(x)$ as

$$E_z^{\text{MoM}} = -\frac{\omega\mu}{4}\int_0^a J_z^{\text{MoM}}(x)\xi(x)H_0^{(2)}(k_0\rho(x))\mathrm{d}x \tag{33}$$

where $J_z^{\text{MoM}}(x)$ is the surface current obtained by solving the matrix of MoM. The piecewise constant function is selected as the basis function of MoM, and the point-matching method is implemented. The mesh size of MoM is set to $\lambda/10$ for accuracy, where λ is a wavelength.

Similarly, for the PO calculation, the z component of the scattered electric field E_z^{PO} is calculated by (5) as

$$E_z^{\text{PO}} = -\frac{\omega\mu}{4}\int_0^a J_z^{\text{PO}}(x)\xi(x)H_0^{(2)}(k_0\rho(x))\mathrm{d}x \tag{34}$$

where $J_z^{\text{PO}}(x)$ is obtained by (3). The mesh size of PO is set to $\lambda/10$ as well.

For the Fraunhofer approximation, the Hankel function in (34) can be approximated by (47) mentioned in Appendix A. By substituting (3), (4), and (47) into (34), the z component of the scattered electric field $E_z^{\text{Fraunhofer}}$ can be calculated analytically as

$$E_z^{\text{Fraunhofer}} = \frac{-E_0\sin\phi' e^{\mathrm{j}\frac{\pi}{4}}}{\sqrt{2}}e^{-\mathrm{j}k_0\left(\rho_s+\frac{a}{2}\cos\phi_0\right)}\frac{k_0 a}{\sqrt{\pi k_0\rho_s}} \times \operatorname{sinc}\left(\frac{k_0 a}{2\pi}(\cos\phi_s-\cos\phi_0)\right) \tag{35}$$

TABLE 1. Simulation Parameters.

Parameters	Scenario 1	Scenario 2	Scenario 3
E_0 (V/m)	1	1	1
f (GHz)	300	[100, 300]	300
a (m)	0.5	0.3, 0.5	0.3, 0.5
ϕ' (°)	60, 90	90	90
ϕ_0 (°)	30, 60	30	30, 60, 90, 120, 150
ϕ_s (°)	30, 60	30	[0, 180]
ρ_s (m)	[0.1, 20]	1	1, 10

where the function sinc(·) is explained in Appendix B.

For the Fresnel approximation, the Hankel function in (34) can be approximated by (53) mentioned in Appendix A. By substituting (3), (4), and (53) into (34), the z component of the scattered electric field E_z^{Fresnel} has a closed-form solution as

$$E_z^{\text{Fresnel}} = \frac{-E_0\sin\phi' e^{\mathrm{j}\frac{\pi}{4}}}{\sqrt{2}}e^{-\mathrm{j}k_0\left(\rho_s+\frac{a}{2}\cos\phi_0-\frac{\rho_s(\cos\phi_s-\cos\phi_0)^2}{2\sin^2\phi_s}\right)} \times \frac{\{C(t_1)-\mathrm{j}S(t_1)\}-\{C(t_2)-\mathrm{j}S(t_2)\}}{|\sin\phi_s|} \tag{36}$$

with

$$t_{1,2} = \sqrt{\frac{k_0\rho_s}{\pi}}\left(\frac{\cos\phi_0-\cos\phi_s}{\sin\phi_s}\pm\frac{a}{2\rho_s}\sin\phi_s\right) \tag{37}$$

where functions $S(\cdot)$ and $C(\cdot)$ are explained in Appendix B.

Finally, for the proposal, the z component of the scattered electric field E_z^{Proposal} is calculated by (32) as

$$E_z^{\text{Proposal}} = \begin{cases} E_L^{\text{d}}+E_R^{\text{d}}, & (\phi_0<\phi_1) \\ E_R^{\text{d}}+E^{\text{r}}/2, & (\phi_0=\phi_1) \\ E_L^{\text{d}}+E_R^{\text{d}}+E^{\text{r}}, & (\phi_1<\phi_0<\phi_2) \\ E_L^{\text{d}}+E^{\text{r}}/2, & (\phi_0=\phi_2) \\ E_L^{\text{d}}+E_R^{\text{d}}, & (\phi_0>\phi_2) \end{cases} \tag{38}$$

The simulation parameters are summarized in Table 1. The magnitude of the electric field at the source is set to 1 V/m. The frequency f is selected in the THz band, i.e., $100-300$ GHz. Continuous wave (CW) with perpendicular polarization is assumed in simulations. The width of RIS is chosen as $0.3-0.5$ m. Both normal incidence and oblique incidence are considered, i.e., $\phi'=90°$ or $\phi'=60°$. The values of ρ_s are designated to $0.1-20$ m by assuming an indoor environment. There are three scenarios assessed in the simulations.

Scenario 1 varies the distance ρ_s from 0.1 m to 20 m with an interval of 0.1 m for the proposal, Fresnel approximation, Fraunhofer approximation, PO, and MoM. There are four cases simulated in scenario 1, i.e., $(\phi', \phi_0, \phi_s) = (60°, 30°, 30°)$, $(\phi', \phi_0, \phi_s) = (60°, 60°, 60°)$, $(\phi', \phi_0, \phi_s) = (90°, 30°, 30°)$, and $(\phi', \phi_0, \phi_s) = (90°, 60°, 60°)$. The accuracy of each method is evaluated in this scenario considering the distance characteristic of RIS.

Scenario 2 changes the frequency f from 100 GHz to 300 GHz with an interval of 1 GHz for the proposal, the Fresnel approximation, the Fraunhofer approximation, PO,

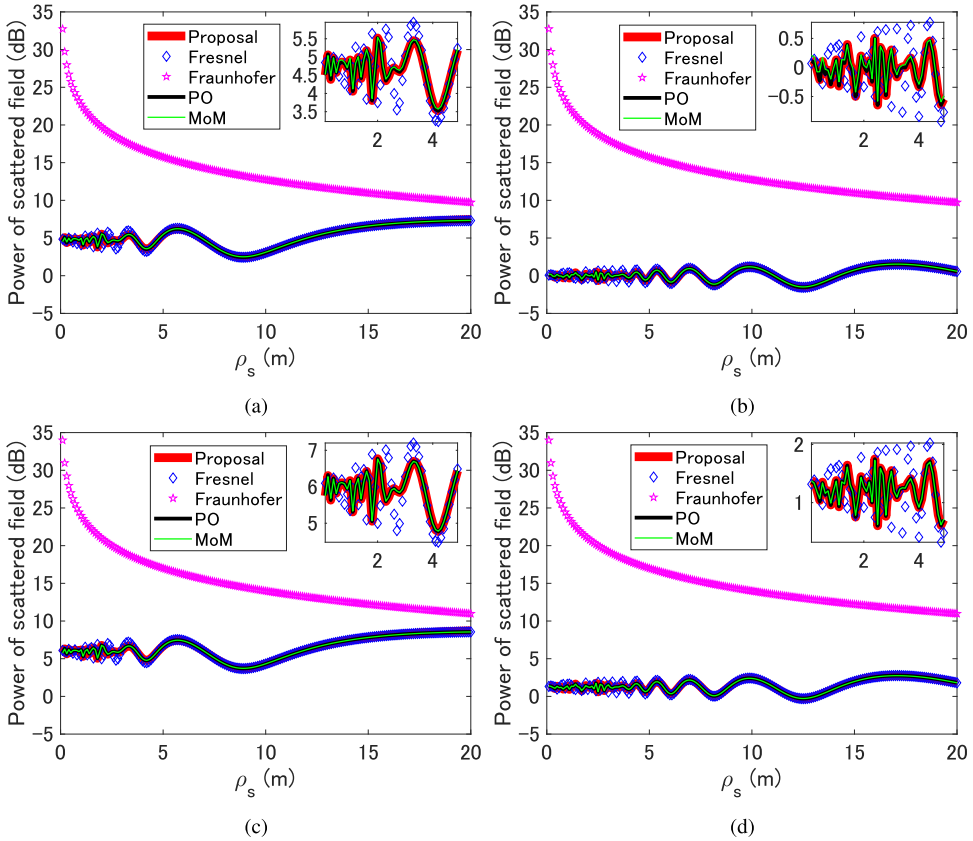

FIGURE 5. Simulated results for scenario 1. The horizontal axis is ρ_s (m). The vertical axis is the power of the scattered electric fields on a dB scale. The red-solid lines, blue-diamond markers, powder-pentagram markers, black-solid lines, and green-solid lines denote the results calculated by the proposal, Fresnel approximation, Fraunhofer approximation, PO, and MoM, respectively. The upper-right subplots zoom in on a portion of curves ($\rho_s \in [0, 5]$ m) and display the zoomed-in results calculated by the proposal, Fresnel approximation, PO, and MoM. (a) Calculated results for the case of (ϕ', ϕ_0, ϕ_s)=(60°, 30°, 30°). (b) Calculated results for the case of (ϕ', ϕ_0, ϕ_s)=(60°, 60°, 60°). (c) Calculated results for the case of (ϕ', ϕ_0, ϕ_s)=(90°, 30°, 30°). (d) Calculated results for the case of (ϕ', ϕ_0, ϕ_s)=(90°, 60°, 60°).

and MoM. There are two cases simulated in scenario 2, i.e., $a = 0.3$ m and $a = 0.5$ m. Scenario 2 compares the computational time of each method with respect to the frequency characteristic.

Scenario 3 alters the observation angle ϕ_s from 0° to 180° with an interval of 1° for $\phi_0 = 30°$, $\phi_0 = 60°$, $\phi_0 = 90°$, $\phi_0 = 120°$, and $\phi_0 = 150°$. Only the proposed method is conducted in scenario 3. There are four cases simulated in scenario 3, i.e., $(a, \rho_s) = (0.3, 1)$ m, $(a, \rho_s) = (0.5, 1)$ m, $(a, \rho_s) = (0.3, 10)$ m, and $(a, \rho_s) = (0.5, 10)$ m. In this scenario, the radiation pattern of RIS is viewed, and the angular characteristic of RIS is discussed.

The processor of the calculating computer is an Intel Core i9-12900K CPU @ 3.19 GHz. The usable installed memory of the calculation computer is 63.7 GB. The system type of the calculating computer is a 64-bit operating system with an x64-based processor. The simulation software is MATLAB.

IV. RESULTS AND DISCUSSIONS

To evaluate the performance of RIS, the power of the scattered electric field is calculated on a decibel (dB) scale. Figures 5, 6, and 7 display the simulated results for scenarios 1, 2, and 3, respectively.

The objective of the results in Fig. 5 is to evaluate the accuracy of each method regarding the distance. The aim of the results in Fig. 6 is to compare the computational cost of each method. The purpose of the results in Fig. 7 is to discuss the radiation pattern of RIS.

The distance characteristic of RIS is shown in Fig. 5. The proposal agrees well with PO and MoM for all results. This work assumes the near-field region by considering the $\lambda/8$-criterion condition (52) mentioned in Appendix A. Accordingly, the range of the near-field region is calculated as approximately $\rho_s \leq 5$ m, as shown in the subplots of Figs. 5(a)-5(d), where there are a few dependencies between the Fresnel approximation and the other (i.e., Proposal, PO, and MoM). The error between the full-wave MoM and the other (i.e., Proposal, Fresnel approximation, Fraunhofer approximation, and PO) is evaluated in the near-field region. The maximum value of the errors for the proposal, the Fresnel approximation, the Fraunhofer approximation, and PO are 0.14 dB, 1.82 dB, 32.61 dB, and 0.15 dB, respectively. Therefore, compared to MoM, the proposal and PO achieve good accuracy with a low error of less than 1 dB, while Fresnel and Fraunhofer approximations present imperfect accuracy with an error of larger than 1 dB in the near-field region.

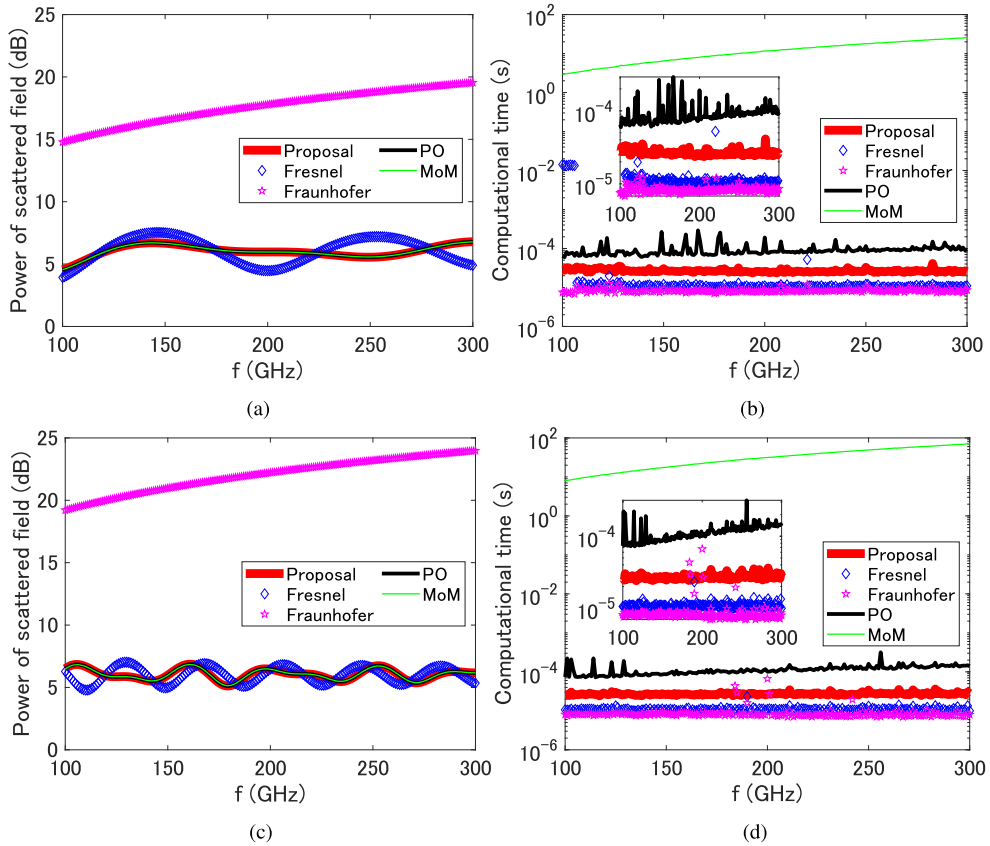

FIGURE 6. Simulated results for scenario 2. The horizontal axis is f (GHz). The red-solid lines, blue-diamond markers, powder-pentagram markers, black-solid lines, and green-solid lines denote the results calculated by the proposal, Fresnel approximation, Fraunhofer approximation, PO, and MoM, respectively. (a) Calculated power of the scattered electric fields on a dB scale under the condition of $a = 0.3$ m. (b) Measured computational time (s) on a logarithmic scale for (a). (c) Calculated power of the scattered electric fields on a dB scale under the condition of $a = 0.5$ m. (d) Measured computational time (s) on a logarithmic scale for (c). The subplots in (b) and (d) display the zoomed-in results calculated by the proposal, Fresnel approximation, Fraunhofer approximation, and PO.

The frequency characteristic of RIS is shown in Fig. 6. The results plotted in Figs. 6(a) and 6(c) also show that the proposal is in good agreement with PO and MoM. Moreover, their computational time is shown in Figs. 6(b) and 6(d), respectively. For the case of $a = 0.3$ m, the average values of the computational time of the proposal, Fresnel approximation, Fraunhofer approximation, PO, and MoM are 0.0268 ms, 0.4857 ms, 0.0083 ms, 0.0915 ms, and 1237.9 ms, respectively. For the case of $a = 0.5$ m, the average values of the computational time of the proposal, the Fresnel approximation, the Fraunhofer approximation, PO, and MoM are 0.0272 ms, 0.0109 ms, 0.0088 ms, 0.1144 ms, and 3412.5 ms, respectively. Therefore, the proposal outperforms PO in terms of calculation speed by approximately $70\% - 76\%$, and the computational time of the proposal is improved by around $46,190 - 125,460$ times by comparing it with MoM. Furthermore, the computational complexity of each method is evaluated and compared. Suppose N is the number of sampling points for PO and MoM, and MoM applies the conjugate gradient method [35] to solve the matrix. By letting C^{Proposal}, C^{Fresnel}, $C^{\text{Fraunhofer}}$, C^{PO}, and C^{MoM} be the computational complexities of the proposal, Fresnel approximation, Fraunhofer approximation, PO, and MoM, respectively, we have

$$C^{\text{Proposal}} \sim O\left(N^0\right), \tag{39a}$$

$$C^{\text{Fresnel}} \sim O\left(N^0\right), \tag{39b}$$

$$C^{\text{Fraunhofer}} \sim O\left(N^0\right), \tag{39c}$$

$$C^{\text{PO}} \sim O(N), \tag{39d}$$

$$C^{\text{MoM}} \sim O\left(N^2\right) \tag{39e}$$

where $O(\cdot)$ is the notation of the order. Since N is proportional to the frequency and the scale of RIS as

$$N = \frac{a}{\frac{\lambda}{10}} \sim af, \tag{40}$$

the computational complexities of PO and MoM become larger with an increase in a or f, while the computational complexities of the proposal, Fresnel approximation, and Fraunhofer approximation are constant. From the results shown in Figs. 6(b) and 6(d), only the computational time of PO and MoM has a tendency to increase proportionally to

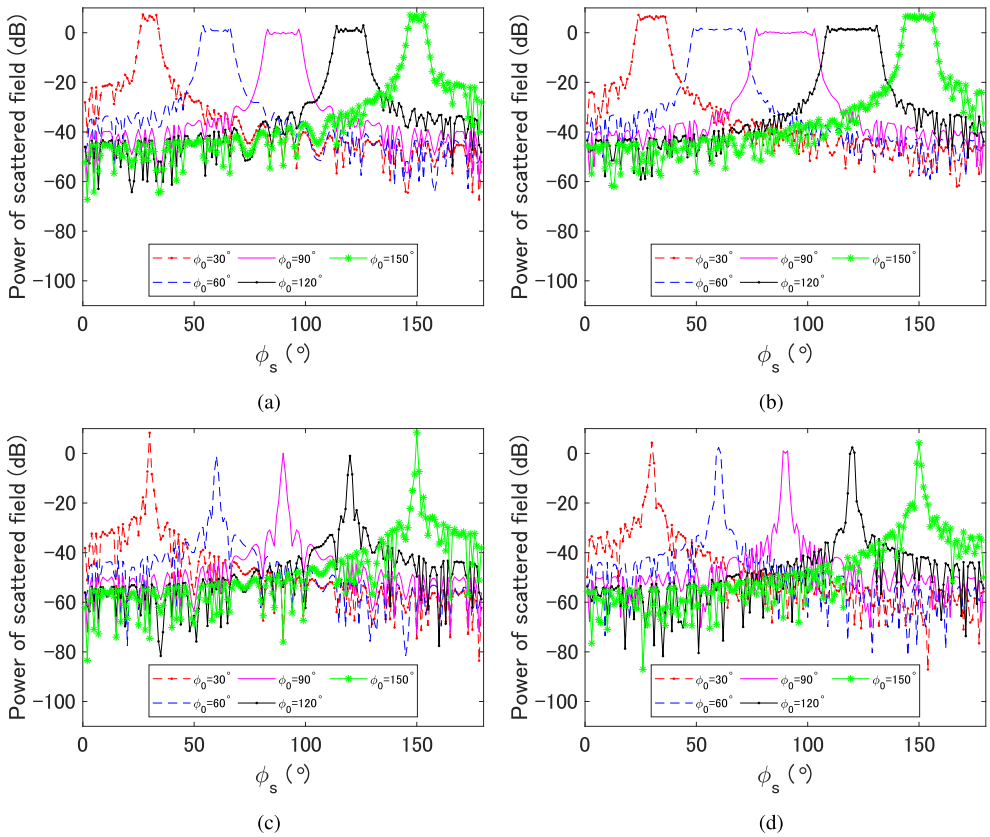

FIGURE 7. Simulated results for scenario 3. The horizontal axis is ϕ_s (°). The vertical axis is the power of the scattered electric fields on a dB scale calculated by the proposal. The red-dash-dotted, blue-dash, powder-solid, black-solid-dotted, and green-solid-asterisk lines denote the results for the desired reflection directions with $\phi_0 = 30°$, $\phi_0 = 60°$, $\phi_0 = 90°$, $\phi_0 = 120°$, and $\phi_0 = 150°$, respectively. (a) Calculated results under the conditions of $a = 0.3$ m and $\rho_s = 1$ m. (b) Calculated results under the conditions of $a = 0.5$ m and $\rho_s = 1$ m. (c) Calculated results under the conditions of $a = 0.3$ m and $\rho_s = 10$ m. (d) Calculated results under the conditions of $a = 0.5$ m and $\rho_s = 10$ m.

the size of RIS or the frequency. The subplots in Figs. 6(b) and 6(d) clearly show the tendency of PO.

The angular characteristic of RIS is plotted in Fig. 7. The results demonstrate that the proposed method is capable of accurately predicting the radiation pattern of RIS, with the direction of the main lobe being in line with the desired reflection direction ϕ_0. In addition, the beam width and side-lobe level [20], [21] of RIS can also be acquired under different conditions. Therefore, the proposal can be utilized to accurately and quickly calculate the coverage of RIS and evaluate unwanted emissions.

From the above results, the proposal can achieve good accuracy with a low error of less than 1 dB, while the Fresnel and Fraunhofer approximations present imperfect accuracy with an error of greater than 1 dB. Moreover, the proposal outperforms PO with a faster calculation speed of approximately $70\% - 76\%$, and the computational time of the proposal is improved by around $46,190 - 125,460$ times by comparing it with MoM. Furthermore, the computational complexity of the proposal is $O(N^0)$, while the computational complexities of PO and MoM are $O(N)$ and $O(N^2)$, respectively. The proposal can produce a fast and accurate prediction of the RIS radiation pattern in, not only the Fraunhofer and Fresnel regions, but also the near-field region.

V. CONCLUSION

This paper proposed a UTD-type solution of PO for RIS modeled by a continuous planar surface in a 2D environment. The authors validated the proposal under different scenarios in an indoor environment ($0.1 - 20$ m) at the THz bands ($100-300$ GHz), comparing with the Fresnel approximation, Fraunhofer approximation, PO, and MoM. The simulated results showed that compared to MoM, the proposal and PO achieved good accuracy with a low error of less than 1 dB, while the Fresnel and Fraunhofer approximations presented imperfect accuracy with an error of greater than 1 dB in the near-field region. Moreover, the proposal outperformed PO with a faster calculation speed of approximately $70\% - 76\%$, and the computational time of the proposal was improved by around $46,190 - 125,460$ times by comparing it with MoM. Furthermore, the computational complexities of the proposal, the Fresnel approximation, and the Fraunhofer approximation were $O(N^0)$, while the computational complexities of PO and MoM were $O(N)$ and $O(N^2)$, respectively. Therefore, the proposal has achieved a good balance between accuracy and computational cost.

As a limitation of this work, the current proposal only considers the 2D environment. Validation is only done by full-wave simulation without the experimental measurements. In this work, the RIS is modeled by a continuous

planar surface, which makes it easy to design a useful formulation, while it may not be practical to evaluate the performance of the specific RIS.

In the future, measurement will be conducted in a three-dimensional (3D) environment to further evaluate the proposal. Several reconfigurable components, including a positive-intrinsic-negative (PIN) diode, varactor diode, and liquid crystal will be used in measurements and will be compared against the proposal with a continuous planar surface.

APPENDIX A
FRAUNHOFER AND FRESNEL APPROXIMATIONS

For the model shown in Fig. 4, the distance from the arbitrary point $(x, 0)$ of RIS to Rx (x_0, y_0) can be expanded by the Taylor series as

$$\rho(x) = \rho_s - \left(x - \frac{a}{2}\right)\cos\phi_s + \frac{\left(x - \frac{a}{2}\right)^2 \sin^2\phi_s}{2\rho_s} + \frac{\left(x - \frac{a}{2}\right)^3 \sin^2\phi_s \cos\phi_s}{2\rho_s^2} + \cdots \tag{41}$$

where a, ρ_s, and ϕ_s are the size of RIS, distance, and observation angle from the center of RIS to Rx, respectively.

A. FRAUNHOFER APPROXIMATION

In the Fraunhofer approximation, only the first order of $x - a/2$ remains as

$$\rho(x) \approx \rho_s - \left(x - \frac{a}{2}\right)\cos\phi_s \tag{42}$$

given that the condition of $(x - a/2)^2 \sin^2\phi_s/(2\rho_s) \to 0$ is held.

For $\lambda/16$-criterion condition [24], we have

$$\frac{\left(x - \frac{a}{2}\right)^2 \sin^2\phi_s}{2\rho_s} < \frac{\lambda}{16} \Rightarrow \rho_s > \frac{8}{\lambda}\left(x - \frac{a}{2}\right)^2 \sin^2\phi_s. \tag{43}$$

To satisfy the maximum value of the right-hand side of (43), the $\lambda/16$-criterion condition of the Fraunhofer approximation is

$$\rho_s > \frac{2a^2}{\lambda}. \tag{44}$$

For $\lambda/8$-criterion condition [46], we have

$$\frac{\left(x - \frac{a}{2}\right)^2 \sin^2\phi_s}{2\rho_s} < \frac{\lambda}{8} \Rightarrow \rho_s > \frac{4}{\lambda}\left(x - \frac{a}{2}\right)^2 \sin^2\phi_s. \tag{45}$$

To satisfy the maximum value of the right-hand side of (45), the $\lambda/8$-criterion condition of the Fraunhofer approximation is

$$\rho_s > \frac{a^2}{\lambda}. \tag{46}$$

From (43), the Hankel function becomes

$$H_0^{(2)}(k_0\rho(x)) \approx \sqrt{\frac{2}{\pi k_0 \rho_s}} e^{j\frac{\pi}{4}} e^{-jk_0\left(\rho_s - \left(x - \frac{a}{2}\right)\cos\phi_s\right)}. \tag{47}$$

B. FRESNEL APPROXIMATION

In the Fresnel approximation, the first and second orders of $x - a/2$ remain as

$$\rho(x) = \rho_s - \left(x - \frac{a}{2}\right)\cos\phi_s + \frac{\left(x - \frac{a}{2}\right)^2 \sin^2\phi_s}{2\rho_s} \tag{48}$$

given that the condition of $(x - a/2)^3 \sin^2\phi_s \cos\phi_s/(2\rho_s^2) \to 0$ is held.

For $\lambda/16$-criterion condition [24], we have

$$\frac{\left(x - \frac{a}{2}\right)^3 \sin^2\phi_s \cos\phi_s}{2\rho_s^2} < \frac{\lambda}{16} \Rightarrow \rho_s > \sqrt{\frac{8}{\lambda}\left(x - \frac{a}{2}\right)^3 \sin^2\phi_s \cos\phi_s}. \tag{49}$$

To satisfy the maximum value of the right-hand side of (49), the $\lambda/16$-criterion condition of the Fresnel approximation is

$$\rho_s > 0.62\sqrt{\frac{a^3}{\lambda}}. \tag{50}$$

Note that the maximum value of $\sin^2\phi_s \cos\phi_s$ is 0.38.

For $\lambda/8$-criterion condition [46], we have

$$\frac{\left(x - \frac{a}{2}\right)^3 \sin^2\phi_s \cos\phi_s}{2\rho_s^2} < \frac{\lambda}{8} \Rightarrow \rho_s > \sqrt{\frac{4}{\lambda}\left(x - \frac{a}{2}\right)^3 \sin^2\phi_s \cos\phi_s}. \tag{51}$$

To satisfy the maximum value of the right-hand side of (51), the $\lambda/8$-criterion condition of the Fresnel approximation is

$$\rho_s > 0.62\sqrt{\frac{a^3}{2\lambda}}. \tag{52}$$

From (48), the Hankel function becomes

$$H_0^{(2)}(k_0\rho(x)) \approx \sqrt{\frac{2}{\pi k_0 \rho_s}} e^{j\frac{\pi}{4}} e^{-jk_0\left(\rho_s - \left(x - \frac{a}{2}\right)\cos\phi_s + \frac{\left(x - \frac{a}{2}\right)^2 \sin^2\phi_s}{2\rho_s}\right)}. \tag{53}$$

APPENDIX B
SPECIAL FUNCTIONS

The function $F(\cdot)$ is a modified Fresnel integral defined as

$$F(t) = j2\sqrt{t}e^{jt}\int_{\sqrt{t}}^{\infty} e^{-j\tau^2} d\tau. \tag{54}$$

When the argument t is small $(t < 1)$

$$F(t) \approx \left(\sqrt{\pi t} - 2e^{j\frac{\pi}{4}}t - \frac{2}{3}e^{-j\frac{\pi}{4}}t^2\right)e^{j\left(\frac{\pi}{4} + t\right)}, \tag{55}$$

and when t is large $(t > 2)$

$$F(t) \approx 1 + j\frac{1}{2t} - \frac{3}{4t^2} - j\frac{15}{8t^3} + \frac{75}{16t^4}. \tag{56}$$

The function sinc(·) is defined as

$$\mathrm{sinc}(t) = \begin{cases} \dfrac{\sin \pi t}{\pi t}, & (t \neq 0) \\ 1, & (t = 0) \end{cases} \tag{57}$$

Functions $S(\cdot)$ and $C(\cdot)$ denote the Fresnel sine and cosine integrals, respectively, defined as

$$S(t) = \int_0^t \sin\left(\frac{\pi \tau^2}{2}\right) \mathrm{d}\tau, \tag{58a}$$

$$C(t) = \int_0^t \cos\left(\frac{\pi \tau^2}{2}\right) \mathrm{d}\tau. \tag{58b}$$

When the argument t is close to zero ($|t| < 1$)

$$S(t) \approx \frac{\pi t^3}{6}, \tag{59a}$$

$$C(t) \approx t - \frac{\pi^2 t^5}{40} \tag{59b}$$

and when $|t|$ is large ($|t| > 2$)

$$S(t) \approx \frac{\mathrm{sgn}(t)}{2} - \left(\frac{1}{\pi t} - \frac{3}{\pi^3 t^5}\right) \cos \frac{\pi t^2}{2} - \frac{\sin \frac{\pi t^2}{2}}{\pi^2 t^3}, \tag{60a}$$

$$C(t) \approx \frac{\mathrm{sgn}(t)}{2} + \left(\frac{1}{\pi t} - \frac{3}{\pi^3 t^5}\right) \sin \frac{\pi t^2}{2} - \frac{\cos \frac{\pi t^2}{2}}{\pi^2 t^3} \tag{60b}$$

where sgn(·) is the sign function.

APPENDIX C
FORMULATIONS IN PARALLEL POLARIZATION

Due to space limitation, only the UTD-type solution of PO for the scattering with parallel polarization contributed from the left edge of a semi-infinite RIS ($a \to \infty$) is derived. The z component of the incident magnetic field H_z^{i} at the arbitrary point $(x, 0)$ of RIS is

$$H_z^{\mathrm{i}}(x) = H_0 e^{\mathrm{j}k_0 x \cos \phi'} \tag{61}$$

where H_0 is the z component of the incident magnetic field at the origin. The PO current is

$$\boldsymbol{J}^{\mathrm{PO}}(x) = 2\hat{y} \times \left(H_z^{\mathrm{i}}(x)\hat{z}\right) = 2H_0 e^{\mathrm{j}k_0 x \cos \phi'} \hat{x}. \tag{62}$$

The z component of the scattered magnetic field H_1^{s} contributed from the left edge of RIS is calculated by using the phase shift $\xi(x)$ in (4) and the normal derivative of the Green function $\partial G(x)/\partial \hat{y}$ as

$$\begin{aligned} H_1^{\mathrm{s}} &= \int_0^\infty J_{\mathrm{x}}^{\mathrm{PO}}(x)\xi(x)\frac{\partial}{\partial \hat{y}} G(x) \mathrm{d}x \\ &= -\frac{\mathrm{j}H_0}{2} \int_0^\infty e^{-\mathrm{j}k_0 x \cos \phi_0} \frac{\partial}{\partial \hat{y}} H_0^{(2)}(k_0 \rho(x)) \mathrm{d}x. \end{aligned} \tag{63}$$

Here, the angular spectral representation of the normal derivative of the Hankel function [39] is

$$\frac{\partial}{\partial \hat{y}} H_0^{(2)}(k_0 \rho(x)) = \frac{\mathrm{j}}{\pi} \int_{-\infty}^{\infty} e^{-\mathrm{j}(k_{\mathrm{x}}(x_0 - x) + k_{\mathrm{y}} y_0)} \mathrm{d}k_{\mathrm{x}}. \tag{64}$$

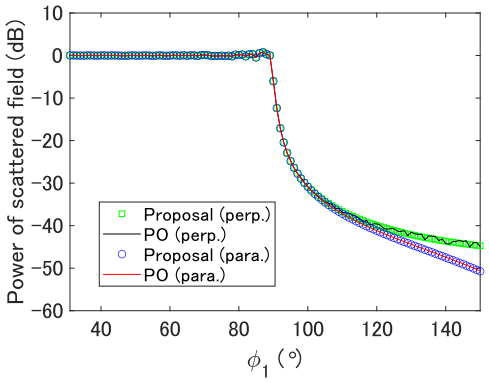

FIGURE 8. Simulated results for different polarization. The horizontal axis is ϕ_1 (°). The vertical axis is the power of the scattered electric fields on a dB scale. The green-square markers, black-solid lines, blue-circle markers, and red-solid lines denote the results calculated by the proposal in perpendicular polarization, PO in perpendicular polarization, proposal in parallel polarization, and PO in parallel polarization, respectively.

By substituting (64) into (63) and interchanging the order of integration, we have

$$\begin{aligned} H_1^{\mathrm{s}} &= \frac{H_0}{2\pi} \int_{-\infty}^{\infty} \left(\int_0^\infty e^{-\mathrm{j}k_0 x \cos \phi_0} e^{\mathrm{j}k_{\mathrm{x}} x} \mathrm{d}x \right) \\ &\quad \times \; e^{-\mathrm{j}(k_{\mathrm{x}} x_0 + k_{\mathrm{y}} y_0)} \mathrm{d}k_{\mathrm{x}} \\ &= \frac{\mathrm{j}H_0}{2\pi} \int_{-\infty}^{\infty} \frac{e^{-\mathrm{j}(k_{\mathrm{x}} x_0 + k_{\mathrm{y}} y_0)}}{k_{\mathrm{x}} - k_0 \cos \phi_0} \mathrm{d}k_{\mathrm{x}}. \end{aligned} \tag{65}$$

By applying (1) and (13a), (65) now reads

$$\begin{aligned} H_1^{\mathrm{s}} &= \frac{\mathrm{j}H_0}{2\pi} \int_\Gamma \frac{-e^{-\mathrm{j}k_0 \rho_1 \cos(\phi_1 - k_\phi)}}{\cos k_\phi - \cos \phi_0} \mathrm{d}k_\phi \\ &= \frac{\mathrm{j}H_0}{4\pi} \int_\Gamma \left(\cot \frac{k_\phi + \phi_0}{2} + \cot \frac{k_\phi - \phi_0}{2} \right) \\ &\quad \times \; e^{-\mathrm{j}k_0 \rho_1 \cos(\phi_1 - k_\phi)} \mathrm{d}k_\phi. \end{aligned} \tag{66}$$

The integral over SDP_1 passing through SPP_1 at ϕ_1 can be evaluated by (17). The contribution of the pole at ϕ_0 enclosed by Γ and SDP_1 can be evaluated by (22) and (23). From (17), (22), and (23), H_1^{s} in (66) can be calculated as

$$H_1^{\mathrm{s}} = \begin{cases} H_1^{\mathrm{r}} + H_1^{\mathrm{d}}, & (\phi_1 < \phi_0) \\ H_1^{\mathrm{d}}, & (\phi_1 > \phi_0) \end{cases} \tag{67}$$

with

$$H_1^{\mathrm{d}} = H_z^{\mathrm{i}}(x_1)\xi(x_1) D_{\parallel}^{\mathrm{RIS}}(\rho_1, \phi_1, \phi_0) \frac{e^{-\mathrm{j}k_0 \rho_1}}{\sqrt{\rho_1}}, \tag{68a}$$

$$H_1^{\mathrm{r}} = H_z^{\mathrm{i}}(x_1)\xi(x_1) R_{\parallel}^{\mathrm{RIS}} e^{-\mathrm{j}k_0 \rho_1 \cos(\phi_1 - \phi_0)} \tag{68b}$$

where H_1^{d} and H_1^{r} denote the complex amplitudes of the diffracted and reflected magnetic fields, respectively. The uniform PO diffraction coefficient $D_{\parallel}^{\mathrm{RIS}}$ and reflection coefficient $R_{\parallel}^{\mathrm{RIS}}$ for the scattering from RIS in parallel polarization

are calculated as

$$D_{\parallel}^{\mathrm{RIS}}(\rho,\phi,\phi_0)=\frac{e^{-\mathrm{j}\frac{\pi}{4}}}{\sqrt{8\pi k_0}}\times\left(\cot\frac{\phi-\phi_0}{2}F\left(2k_0\rho\sin^2\frac{\phi-\phi_0}{2}\right)+\cot\frac{\phi+\phi_0}{2}F\left(2k_0\rho\sin^2\frac{\phi+\phi_0}{2}\right)\right),\tag{69a}$$

$$R_{\parallel}^{\mathrm{RIS}}=1.\tag{69b}$$

The proposal is validated by comparing it with PO [47]. Figure 8 shows the simulated results under the conditions of $E_0 = 1$ V/m, $f = 300$ GHz, $\phi' = 90°$, $\phi_0 = 90°$, and $\rho_1 = 1$ m in both perpendicular polarization and parallel polarization, when the observation angle ϕ_1 is varied from 30° to 150°. The results demonstrate that the proposal is in agreement with PO in both perpendicular and parallel polarizations.

REFERENCES

[1] M. Di Renzo et al., "Smart radio environments empowered by reconfigurable intelligent surfaces: How it works, state of research, and the road ahead," *IEEE J. Sel. Areas Commun.*, vol. 38, no. 11, pp. 2450–2525, Nov. 2020.

[2] C. Huang, R. Mo, and C. Yuen, "Reconfigurable intelligent surface assisted multiuser MISO systems exploiting deep reinforcement learning," *IEEE J. Sel. Areas Commun.*, vol. 38, no. 8, pp. 1839–1850, Aug. 2020.

[3] Y. Liu et al., "Reconfigurable intelligent surfaces: Principles and opportunities," *IEEE Commun. Surv. Tutor.*, vol. 23, no. 3, pp. 1546–1577, 3rd Quart., 2021.

[4] X. Liu, Y. Liu, Y. Chen, and H. V. Poor, "RIS enhanced massive non-orthogonal multiple access networks: Deployment and passive beamforming design," *IEEE J. Sel. Areas Commun.*, vol. 39, no. 4, pp. 1057–1071, Apr. 2021.

[5] S. Gong et al., "Toward smart wireless communications via intelligent reflecting surfaces: A contemporary survey," *IEEE Commun. Surv. Tutor.*, vol. 22, no. 4, pp. 2283–2314, 4th Quart., 2020.

[6] C. Pan et al., "Intelligent reflecting surface aided MIMO broadcasting for simultaneous wireless information and power transfer," *IEEE J. Sel. Areas Commun.*, vol. 38, no. 8, pp. 1719–1734, Aug. 2020.

[7] S. Zhang and R. Zhang, "Capacity characterization for intelligent reflecting surface aided MIMO communication," *IEEE J. Sel. Areas Commun.*, vol. 38, no. 8, pp. 1823–1838, Aug. 2020.

[8] J. C. B. Garcia, A. Sibille, and M. Kamoun, "Reconfigurable intelligent surfaces: Bridging the gap between scattering and reflection," *IEEE J. Sel. Areas Commun.*, vol. 38, no. 11, pp. 2538–2547, Nov. 2020.

[9] B. Zheng, C. You, W. Mei, and R. Zhang, "A survey on channel estimation and practical passive beamforming design for intelligent reflecting surface aided wireless communications," *IEEE Commun. Surv. Tutor.*, vol. 24, no. 2, pp. 1035–1071, 2nd Quart., 2022.

[10] E. Basar, M. Di Renzo, J. De Rosny, M. Debbah, M.-S. Alouini, and R. Zhang, "Wireless communications through reconfigurable intelligent surfaces," *IEEE Access*, vol. 7, pp. 116753–116773, 2019.

[11] Ö. Özdogan, E. Björnson, and E. G. Larsson, "Intelligent reflecting surfaces: Physics, propagation, and pathloss modeling," *IEEE Wirel. Commun.*, vol. 9, no. 5, pp. 581–585, May 2020.

[12] M. Di Renzo, F. Habibi Danufane, X. Xi, J. de Rosny, and S. Tretyakov, "Analytical modeling of the path-loss for reconfigurable intelligent surfaces—Anomalous mirror or scatterer?," in *Proc. IEEE 21st Int. Workshop Signal Process. Adv. Wireless Commun. (SPAWC)*, 2020, pp. 1–5.

[13] W. Tang et al., "Wireless communications with reconfigurable intelligent surface: Path loss modeling and experimental measurement," *IEEE Trans. Wireless Commun.*, vol. 20, no. 1, pp. 421–439, Jan. 2021.

[14] S. W. Ellingson, "Path loss in reconfigurable intelligent surface-enabled channels," in *Proc. IEEE 32nd Annu. Int. Symp. Per., Indoor Mobile Radio Commun. (PIMRC)*, 2021, pp. 829–835.

[15] E. Björnson and L. Sanguinetti, "Demystifying the power scaling law of intelligent reflecting surfaces and metasurfaces," in *Proc. IEEE 8th Int. Workshop Comput. Adv. Multi-Sensor Adapt. Process. (CAMSAP)*, 2019, pp. 549–553.

[16] S. Hu, F. Rusek, and O. Edfors, "Beyond massive MIMO: The potential of data transmission with large intelligent surfaces," *IEEE Trans. Signal Process.*, vol. 66, no. 10, pp. 2746–2758, May 2018.

[17] D. Davide, "Communicating With large intelligent surfaces: Fundamental limits and models," *IEEE J. Sel. Areas Commun.*, vol. 38, no. 11, pp. 2526–2537, Nov. 2020.

[18] E. Björnson and L. Sanguinetti, "Power scaling laws and near-field behaviors of massive MIMO and intelligent reflecting surfaces," *IEEE Open J. Commun. Soc.*, vol. 1, pp. 1306–1324, 2020.

[19] E. Björnson, Ö. Özdogan, and E. G. Larsson, "Intelligent reflecting surface versus decode-and-forward: How large surfaces are needed to beat relaying?," *IEEE Wireless Commun. Lett.*, vol. 9, no. 2, pp. 244–248, Feb. 2020.

[20] C. L. Dolph, "A current distribution for broadside arrays which optimizes the relationship between beam width and side-lobe level," *Proc. IRE*, vol. 34, no. 6, pp. 335–348, Jun. 1946.

[21] M. M. Khodier and C. G. Christodoulou, "Linear array geometry synthesis with minimum sidelobe level and null control using particle swarm optimization," *IEEE Trans. Antennas Propag.*, vol. 53, no. 8, pp. 2674–2679, Aug. 2005.

[22] Y. Karasawa and H. Iwai, "Enhancement of the ETP model: How to calculate BER due to ISI for wide-band digital transmission in Nakagami-Rice fading environments," *IEEE Trans. Veh. Technol.*, vol. 49, no. 6, pp. 2113–2120, Nov. 2000.

[23] V. Degli-Esposti, E. M. Vitucci, M. D. Renzo, and S. A. Tretyakov, "Reradiation and scattering from a reconfigurable intelligent surface: A general macroscopic model," *IEEE Trans. Antennas Propag.*, vol. 70, no. 10, pp. 8691–8706, Oct. 2022.

[24] T. Imai, A. Kumagai, K. Takahashi, and O. Kagaya, "Proposal on RIS scattering model based on physical-optics approximation," in *Proc. EuCAP*, 2023, pp. 1–5.

[25] P. Y. Ufimtsev, "New insight into the classical Macdonald physical optics approximation," *IEEE Trans. Antennas Propag. Mag.*, vol. 50, no. 3, pp. 11–20, Jun. 2008.

[26] P. Y. Ufimtsev, *Fundamentals of the Physical Theory of Diffraction*, Hoboken, NJ, USA: Wiley, 2013, pp. 1–48.

[27] S. Mukherjee, G. Skidmore, T. Chawla, A. Bhardwaj, C. Gentile, and J. Senic, "Scalable modeling of human blockage at millimeter-wave: A comparative analysis of knife-edge diffraction, the uniform theory of diffraction, and physical optics against 60 GHz channel measurements," *IEEE Access*, vol. 10, pp. 133643–133654, 2022.

[28] J. B. Keller, "Geometric theory of diffraction," *J. Opt. Soc. America*, vol. 52, no. 2, pp. 116–130, 1962.

[29] G. L. James, *Geometrical Theory of Diffraction for Electromagnetic Waves*, Stevenage, U.K.: IET, 1986.

[30] R. G. Kouyoumjian and P. H. Pathak, "A uniform geometrical theory of diffraction for an edge in a perfectly conducting surface," *Proc. IEEE*, vol. 62, no. 11, pp. 1448–1461, Nov. 1974.

[31] M. Born and E. Wolf, *Principles of Optics: Electromagnetic Theory of Propagation, Interference and Diffraction of Light*, Cambridge, U.K.: Cambridge Univ. Press, 2013.

[32] X. Du and J. Takada, "Structure of the field behind a dielectric circular cylinder in the lit side of the transition region," *Prog. Electromagn. Res. M*, vol. 116, no. 9, pp. 103–118, Apr. 2023.

[33] X. Du and J. Takada, "A uniform additional term using Fock-type integral to unify edge diffraction, creeping diffraction, and reflection in lit and shadowed regions," *Prog. Electromagn. Res. B*, vol. 101, no. 6, pp. 101–117, Jul. 2023.

[34] C. A. Balanis, *Advanced Engineering Electromagnetics*, Hoboken, NJ, USA: Wiley, 1989, pp. 767–799.

[35] N. Morita, N. Kumagai, and J. R. Mautz, *Integral Equation Methods for Electromagnetics*, Boston, MA, USA: Artech House Antenna Library, 1990.

[36] Y. L. C. de Jong, "Uniform ray description of physical optics scattering by finite locally periodic metasurfaces," in *Proc. IEEE Trans. Antennas Propag.*, vol. 70, no. 4, pp. 2949–2959, Apr. 2022.

[37] S. Stewart, Y. L. C. de Jong, T. J. Smy, and S. Gupta, "Ray-optical evaluation of scattering from electrically large metasurfaces characterized by locally periodic surface susceptibilities," *IEEE Trans. Antennas Propag.*, vol. 70, no. 2, pp. 1265–1278, Feb. 2022.
[38] G. Gradoni and M. D. Renzo, "End-to-end mutual coupling aware communication model for reconfigurable intelligent surfaces: An electromagnetic-compliant approach based on mutual impedances," *IEEE Wirel. Commun. Lett.*, vol. 10, no. 5, pp. 938–942, May 2021.
[39] J. Ahrens, *Analytic Methods of Sound Field Synthesis*, Berlin, Germany: Springer-Verlag, 2012.
[40] X. Du, K. Saito, J. Takada, and P. Hanpinitsak, "A novel mirror Kirchhoff approximation method for predicting the shadowing effect by a metal cuboid," *Prog. Electromagn. Res. M*, vol. 104, no. 18, pp. 199–212, Sep. 2021.
[41] X. Du and J.-I. Takada, "Mirror Kirchhoff approximation for predicting shadowing effect by a PEC convex cylinder," in *Proc. Appl. Computa. Electromagn. Soci.*, 2021, pp. 1–3.
[42] X. Du and J.-I. Takada, "Low computational cost mirror Kirchhoff approximation for predicting shadowing effect," *IEEE Access*, vol. 10, pp. 23829–23841, 2022.
[43] X. Du and J.-I. Takada, "Design of parameters of fast Fourier transform for three-dimensional split step parabolic equations and mirror Kirchhoff approximation," *IEEE Access*, vol. 11, pp. 44964–44976, 2023.
[44] P. C. Clemmow, "Some extension to the method of integration by steepest descent," *Q. J. Mech. Appl. Math*, vol. 3, no. 2, pp. 241–256, Jan. 1950.
[45] A. V. Osipov and S. A. Tretyakov, *Modern Electromagnetic Scattering Theory with Applications*, Hoboken, NJ, USA: Wiley, 2013, pp. 274–277.
[46] R. Celestre, "Investigations of the effect of optical imperfections on partially coherent X-ray beam by combining optical simulations with wavefront sensing experiments," Ph.D. dissertation, Phys. Condens. Matter Radiat., Université Grenoble Alpes, Grenoble, France, 2021, pp. 18–20.
[47] T. Kohama and M. Ando, "Physical optics radiation integrals with frequency-independent number of division utilizing Fresnel zone number localization and adaptive sampling method," *IEICE Trans. Elec.*, vol. 97, no. 12, pp. 1134–1141, 2014.

XIN DU (Member, IEEE) was born in 1992. He received the B.E. degree in international development engineering and the M.S. and D.E. degrees in transdisciplinary science and engineering from the Tokyo Institute of Technology, Tokyo, Japan, in 2017, 2019, and 2022, respectively.

From 2017 to 2019, he was a Research Assistant with the School of Environment and Society, Tokyo Institute of Technology, where he is currently a Postdoctoral Researcher. His research interests include numerical electromagnetic simulation, diffraction theory, and reconfigurable intelligent surfaces.

Dr. Du is a member of the IEICE, Japan.

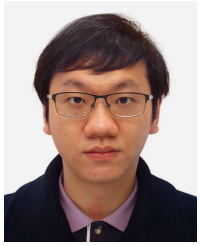

CHECHIA KANG was born in 1995. He received the B.E. degree in international development engineering and the M.S. degree in transdisciplinary science and engineering from the Tokyo Institute of Technology, Tokyo, Japan, in 2019 and 2021, respectively, where he is currently pursuing the D.E. degree.

From 2019 to 2023, he was a Research Assistant with the School of Environment and Society, Tokyo Institute of Technology. His research interests include numerical electromagnetic simulation and measurements of the human shadowing effect.

Mr. Kang is a student member of the IEICE, Japan.

JUN-ICHI TAKADA (Senior Member, IEEE) received the B.E., M.E., and D.E. degrees in electrical and electronic engineering from the Tokyo Institute of Technology, Tokyo, Japan, in 1987, 1989, and 1992, respectively.

He was a Research Associate with Chiba University, Chiba, Japan, from 1992 to 1994, and an Associate Professor with the Tokyo Institute of Technology from 1994 to 2006. He was also a Researcher with the National Institute of Information and Communications Technology, Kanagawa, Japan, from 2003 to 2007. He has been a Professor with the Tokyo Institute of Technology since 2006. His research interests include radio-wave propagation and channel modeling for mobile and short-range wireless systems, regulatory issues of spectrum sharing, and ICT applications for international development.

Prof. Takada is a fellow of the IEICE, Japan.